RESEARCH ARTICLE

Key Points:
- Infrasound waves triggered by seismic activity propagate upward and dissipate in the upper atmosphere and ionosphere
- The propagation of infrasound in the upper atmosphere is nonlinear, and N-shaped pulse is formed if the initial amplitude is large enough
- Numerical simulation based on solution of nonlinear compressible fluid equations is consistent with observation

Correspondence to:
J. Chum,
jachu@ufa.cas.cz

Nonlinear acoustic waves in the viscous thermosphere and ionosphere above earthquake

J. Chum[1] (iD), M. A. Cabrera[2], Z. Mošna[1] (iD), M. Fagre[2] (iD), J. Baše[1], and J. Fišer[1] (iD)

[1]Institute of Atmospheric Physics, Prague, Czech Republic, [2]Laboratorio de Telecomunicaciones, Facultad de Ciencias Exactas y Tecnología, Universidad Nacional de Tucumán, San Miguel de Tucumán, Argentina

Abstract The nonlinear behavior of acoustic waves and their dissipation in the upper atmosphere is studied on the example of infrasound waves generated by vertical motion of the ground surface during the M_w 8.3 earthquake that occurred about 46 km from Illapel, Chile on 16 September 2015. To conserve energy, the amplitude of infrasound waves initially increased as the waves propagated upward to the rarefied air. When the velocities of air particles became comparable with the local sound speed, the nonlinear effects started to play an important role. Consequently, the shape of waveform changed significantly with increasing height, and the original wave packet transformed to the "N-shaped" pulse resembling a shock wave. A unique observation by the continuous Doppler sounder at the altitude of about 195 km is in good agreement with full wave numerical simulation that uses as boundary condition the measured vertical motion of the ground surface.

1. Background

The magnitude M_w 8.3 earthquake started offshore from the Coquimbo region about 46 km west from the Illapel City, Chile on 16 September 2015 at 22:54:32 UT [http://earthquake.usgs.gov/earthquakes/event-page/us20003k7a#general_region]. The earthquake occurred as the result of thrust faulting on the interface between the subducting Nazca plate and South American continent. The epicenter was located at 31.6°S, 71.7°W, and its depth was estimated to 23 km [*Barrientos*, 2015; *Tilmann et al.*, 2016]. The rupture propagated mainly northward with maximum displacement around 6 m. The rupture length reached about 230 km, and the majority of moment was released during approximately 100 s [*Barrientos*, 2015; *Tilmann et al.*, 2016].

Vertical movement of the ground surface produces pressure fluctuations which propagate upward as infrasound waves and might reach the thermosphere and ionosphere [*Bolt*, 1964; *Donn and Postmentier*, 1964; *Davies and Baker*, 1965; *Watada et al.*, 2006; *Chum et al.*, 2012]. Only the long-period infrasound waves, with periods approximately longer than 10 s, are able to reach ionospheric heights, especially the most ionized *F* layer at the altitudes of approximately 150–300 km, in which the waves can be detected by remote sounding techniques. The infrasound waves of shorter periods are strongly attenuated below the *F* layer altitudes and usually do not produce observable disturbances in the ionosphere [*Blanc*, 1985; *Lastovicka et al.*, 2010; *Chum et al.*, 2016]. Sufficiently long period waves are generated only by strong, mostly $M_w > 7$ earthquakes. The investigation of coseismic perturbations in the ionosphere represents a basic research. However, a proper distinguishing of different sources of the ionospheric perturbations and correct understanding of coupling between the solid Earth, ocean, upper atmosphere, and ionosphere could potentially find application in tsunami warning systems [*Rolland et al.*, 2010; *Arai et al.*, 2011; *Kherani et al.*, 2016].

The coseismic perturbations are usually detected from the total electron content (TEC) measurements by dual-frequency GPS receivers [*Calais and Minster*, 1995; *Heki and Ping*, 2005; *Liu et al.*, 2011] and continuous Doppler sounding [*Artru et al.*, 2004; *Liu et al.*, 2006; *Chum et al.*, 2016]. The coseismic perturbations can also be revealed in ionograms if the sounding takes place at proper time [*Maruyama and Shinagawa*, 2014]. The GPS TEC is an integral value measured along the path between the GPS receiver and satellite. It is usually assumed that the main contribution to the TEC variations is at the altitudes around the peak of maximum ionization, approximately from 200 to 300 km, i.e., in the F_2 layer. Therefore, it is impossible to determine the exact height of the TEC disturbances and hence the waveform of air and plasma density fluctuations at a specific altitude. On the other hand, the Doppler sounding provides information about plasma fluctuations at the specific altitude, in which the so called plasma frequency, given by the plasma density, matches the frequency of the sounding radio wave. Recently, it was shown that calculations of air particle velocities from Doppler shifts that are based on an approximation of mirror-like reflection of radio waves from the ionosphere might give wrong results; a

compression of ionospheric plasma owing to infrasound waves has to be considered to calculate the air particle velocities from the observed Doppler shifts [*Chum et al.*, 2016]. The reported Doppler shift measurements were performed several thousand of kilometers from the earthquake epicenter.

Afraimovich et al. [2001] introduced the term "shock-acoustic waves" when analyzing the ionospheric N-shaped TEC perturbations that were generated by four $M_w > 7$ earthquakes and measured by the dual-frequency GPS receivers close to the earthquake epicenters, at distances of several hundreds of kilometers. However, the authors stated that the term shock-acoustic waves did not reflect the physical nature of the phenomenon. They used a linear theory in their analysis, neglected absorption, and summed the contributions of waves generated at different places on the ground. Observations of the N-shaped TEC perturbations in the vicinity of strong earthquakes were later reported, e.g., by *Astafyeva and Heki* [2009], *Astafyeva et al.* [2011], and *Reddy and Seemala* [2015]. The N-shaped disturbances were not observed at distances larger than about 1500 km from the epicenter [*Astafyeva and Heki*, 2009; *Reddy and Seemala*, 2015; *Chum et al.*, 2016]. The importance of nonlinear phenomena on propagation of large amplitude infrasound waves at high altitudes was pointed out by *Krasnov et al.* [2007], who modeled the propagation of sinusoidal signals from a point source.

In this paper, the acoustic waves detected by continuous Doppler sounding as ionospheric fluctuations at the altitude of about 195 km and distance of ~800 km from the epicenter of Illapel earthquake that occurred on 16 September 2015 are compared with the nonlinear numerical simulation of infrasound propagation. The measured vertical velocity of ground surface motion was used as boundary condition in the system of compressible viscous fluid equations. It is shown that nonlinear phenomena are important to explain the observed waveform and that the observed time delay of about 530 s between the vertical motion of the ground surface and the corresponding fluctuations in the ionosphere is consistent with the simulated vertical propagation of infrasound. To the best of our knowledge, it is the first paper in which the formation of the N-shaped waveform in the upper atmosphere and ionosphere above a strong earthquake is described on the basis of direct comparison of measured data in the ionosphere with the results of nonlinear numerical simulation initiated by the measured vertical motion of the ground surface. The paper is organized as follows: section 2 describes the measurements; section 3 provides equations to calculate the air particle velocities from the observed Doppler shifts; section 4 presents the numerical simulation; section 5 discusses the results with respect to the previous reports; and section 6 gives a brief summary.

2. Measurements

The atmospheric fluctuations in the ionosphere were measured via the plasma density changes at a specific height by the continuous Doppler sounding system (CDSS) that operated at a frequency $f_0 = 4.63$ MHz in the Tucumán region, Argentina, about 800 km northeast from the earthquake epicenter. The CDSS actually consists of three transmitters (transmitted power 1 W) that form approximately an equilateral triangle with sides of about 100 km, and one receiver (26.840°S, 65.230°W) located between the transmitters at the city of San Miguel de Tucumán [*Chum et al.*, 2014]. One of the transmitters was not working at the time of earthquake. There is also an ionospheric sounder in San Miguel de Tucumán. Thus, it is possible to determine the electron density profile and hence the reflection height of the sounding radio wave.

The vertical velocity v_z of the ground surface motion was measured by the Guralp-40T seismometer sensor and recorded with the sampling rate of 100 Hz at Horco Molle station (26.784°S, 65.335°W), about 12 km from the Doppler receiver.

Figure 1a shows v_z as a function of time; time $t = 0$ corresponds to the start of the earthquake at 22:54:32 UT. The maximum amplitudes of v_z are observed around $t = 300$ s. Figure 1b presents the ionogram recorded in San Miguel de Tucumán at 23:00 UT. The measured virtual heights are displayed by yellow color and were manually fitted (scaled) and digitized. The digital data were then used as input to the SAO explorer software [*Reinisch et al.*, 2005] to compute the electron density profile (true heights) marked by magenta curve. It can be determined from this electron density profile that ordinary and extraordinary mode for $f_0 = 4.63$ MHz reflected at 198 km and 195 km, respectively. However, the estimated uncertainties of the true heights are about 20 km as their calculation depends not only on the precision of scaling (determination of virtual heights) but also on the electron densities in the "valley" between the E(Es) and *F* layers (heights around
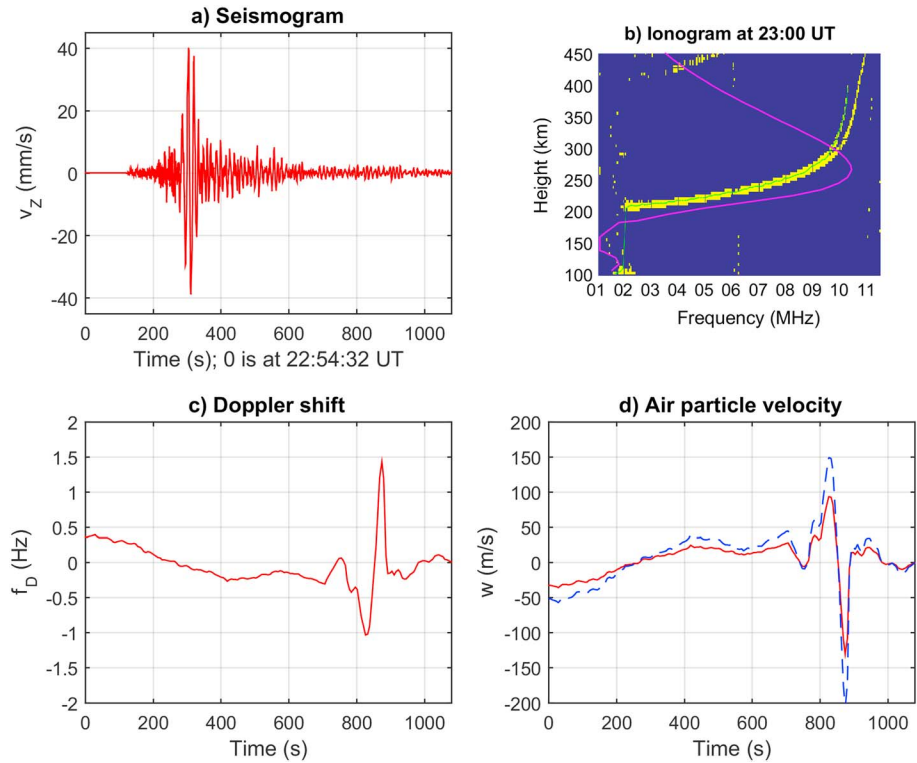
Figure 1. Measurements recorded during the Illapel earthquake. Time=0 corresponds to the beginning of earthquake at 22:54:32 UT on 16 September 2016 in Figures 1a, 1c, and 1d. (a) Vertical velocity v_z of ground surface motion at Tucumán, Horco Molle (latitude=−26.784; longitude=−65.335). (b) Ionogram recorded in Tucumán at 23:00 UT on 16 September 2016. (c) Doppler shift f_D recorded in Tucumán. (d) The air particles velocities w derived from f_D by equation (2) in red and equation (1) in dashed blue.

150 km in Figure 1b). The electron densities in the local minima (valleys between ionospheric layers) are not measurable by ionosonde and are therefore estimated by modeled values, built-in in the SAO explorer software. The obtained true heights depend on the model of the valley. Figure 1c shows the Doppler shift fluctuations measured by the CDSS. The Doppler shifts f_D that are displayed in Figure 1c correspond to the frequencies of maxima of power spectral densities in the original Doppler shift spectrogram that was computed with overlapping time windows. The spectral maxima (f_D values) were determined with the time resolution of 6 s and visually checked/corrected against the original Doppler shift spectrogram. Specifically, mean values of f_D obtained from two working transmitter-receiver pairs are presented for clarity (both f_D signals were almost identical). A distinct coseismic response is observed approximately at times from 800 to 900 s after the start of the earthquake. The time delay between the vertical motion of the ground surface displayed in Figure 1a and the coseismic response drawn in Figures 1c and 1d, obtained by the method described by *Chum et al.* [2016], is about 530 s. The coseismic response has dominant period around 2 min and is superposed on a long-period (around 20 min) fluctuation of f_D caused by a gravity wave.

3. Data Analysis

Air particle oscillation velocities are estimated from the measured Doppler shift values f_D. If the plasma density gradient in the reflection region is very high, then the reflection of radio wave resembles the reflection from a mirror. Consequently, the velocity of air particles, w, for the vertically propagating infrasound waves can be computed by equation (1), provided that the half distance between the Doppler transmitter and receiver is much smaller than the reflection height.

$$w = -f_D \cdot \frac{c}{2f_0 \sin^2(I)}, \tag{1}$$

where c is the speed of light and I is the inclination of magnetic field ($I=27°$ in Tucumán). Equation (1) also

assumes that the plasma is magnetized (plasma can freely move only along the magnetic field lines), which is valid for the heights approximately larger than 130 km [*Rishbeth*, 1997]. The infrasound waves cause the compression and rarefaction of ionospheric plasma. These additional plasma density changes arising from the compression/rarefaction of the air might contribute to the observed Doppler shift significantly [*Chum et al.*, 2016]. In such a case, the vertical air particle velocities should be computed from the experimental data by equation (2)

$$w = -f_D \cdot \frac{c}{2f_0 \sin^2(I)} \cdot \frac{\frac{\partial N}{\partial z}}{\sqrt{\left(\frac{\partial N}{\partial z}\right)^2 + \left(N \frac{2\pi f_{IS}}{c_s}\right)^2}}, \tag{2}$$

where N is the electron (plasma) density, f_{IS} is the infrasound frequency, and c_s is the speed of infrasound propagation. All the terms $\partial N/\partial z$, N, f_{IS}, and c_s are considered at the altitude of observation (reflection of the Doppler signal). The gradient $\partial N/\partial z$ is determined from the electron density profile measured by ionospheric sounder, $\partial N/\partial z \sim 1.4 \cdot 10^7 \, \mathrm{m}^{-4}$. Figure 1d shows the values of w in m/s calculated from the observed f_D values. Red curve is for w computed by equation (2). The dashed blue curve was obtained by equation (1). The w values calculated by equations (1) and (2) differ by several tens of percent. This is different from the previous Doppler observations performed at far distances from the earthquake epicenters, when the $N \cdot (2\pi f_{IS})/c_s$ terms were more than 10 times larger than the $\partial N/\partial z$ terms as f_{IS} was comparable with the frequencies of v_z. Consequently, the w values calculated by equation (1) were unrealistically large, about 10 times larger than those calculated by equation (2) [*Chum et al.*, 2012; *Chum et al.*, 2016]. In the current case, the f_{IS} is relatively low compared to the frequency of v_z, most of the power spectral intensity of f_D (w) is at around 0.008 Hz, and $\partial N/\partial z$ and $N \cdot (2\pi f_{IS})/c_s$ are of the same order. The fluctuations of w have opposite sign than those of f_D because upward movements of air particles and plasma cause negative Doppler shifts, according to equations (1) and (2). The opposite sign is also seen in Figures 1c and 1d.

4. Numerical Simulation

Next, the delay, shape, and amplitude of the observed waveform are compared with the numerical simulation of infrasound propagation. In order to take into account the losses of wave momentum and energy during the infrasound propagation in the upper atmosphere, the set of nonlinear compressible fluid equations with molecular viscosity and thermal conductivity is considered. As the propagation is roughly vertical, the computation is limited to one-dimensional case. The continuity, momentum, and heat equations in one dimension, along the vertical z axis, can be written as follows [*Vadas and Fritts*, 2005]:

$$\frac{\partial \rho_1}{\partial t} = -\frac{\partial(\rho_0 + \rho_1)}{\partial z} w - \frac{\partial w}{\partial z}(\rho_0 + \rho_1), \tag{3}$$

$$\frac{\partial w}{\partial t} = -\frac{\partial w}{\partial z} w - \frac{R(T_0 + T_1)}{(\rho_0 + \rho_1)} \frac{\partial(\rho_0 + \rho_1)}{\partial z} - R \frac{\partial(T_0 + T_1)}{\partial z} - g + \frac{4}{3} \frac{\mu}{(\rho_0 + \rho_1)} \frac{\partial^2 w}{\partial z^2}, \tag{4}$$

$$\frac{\partial T_1}{\partial t} = -\frac{\partial(T_0 + T_1)}{\partial z} w - (\gamma - 1)(T_0 + T_1) \frac{\partial w}{\partial z} + \frac{\gamma \mu}{\mathrm{Pr}(\rho_0 + \rho_1)} \frac{\partial^2 T_1}{\partial z^2}, \tag{5}$$

where ρ_0 and T_0 is the unperturbed air density and temperature, respectively, obtained by the NRLMSISE-00 model for the location and time of measurement, ρ_1 is the density perturbation, T_1 is the temperature perturbation, w is the vertical component of air particle velocity (the unperturbed value is assumed zero), R is the specific gas constant ($R = k_B/m$; k_B is the Boltzmann's constant and m is the mean mass of the air particles), g is the gravitational acceleration, μ is the molecular (dynamic) viscosity, γ is the adiabatic exponent, and Pr is the Prandtl number that relates the molecular viscosity with the thermal conductivity; Pr is approximately 0.7 for the air [*Vadas and Fritts*, 2005]. The values of viscosity of the air μ_A were obtained from the Sutherland formula [*Sutherland and Bass*, 2004] for the undisturbed temperature profile T_0. The values of viscosity of the atomic oxygen μ_O were computed according to *Dalgarno and Smith* [1962]. The values of μ used in equations (4) and (5) were determined as the weighted averages of μ_A and μ_O, according to the relative mass fractions of the atomic oxygen at the specific heights. It should be noted that the values of μ_A and μ_O were within several percent identical. Similarly, the values of adiabatic exponent γ were obtained from the relative mass densities of diatomic gas ($\gamma_A = 7/5$) and monoatomic gas ($\gamma_A = 5/3$). The densities of N_2, O_2
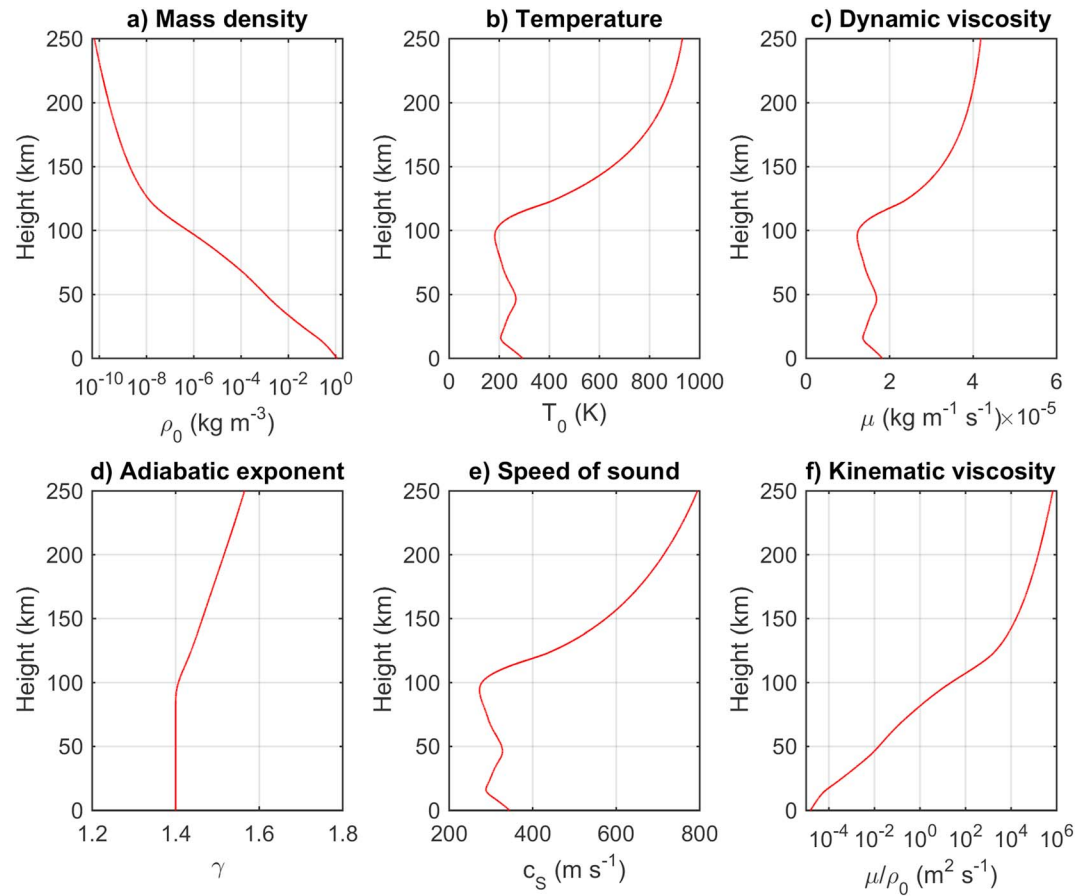
Figure 2. Atmospheric parameters above Tucumán, used in numerical simulation, obtained from NRLMSISE-00 model at 23:00 UT on 16 September. (a) Mass density. (b) Temperature. (c) Dynamic viscosity. (d) Adiabatic exponent. (e) Speed of sound. (f) Kinematic viscosity.

molecules and O atoms were obtained by the NRLMSISE-00 model. Figure 2 shows the dependence of ρ_0, T_0, μ, μ/ρ_0, sound speed c_S, and γ on height.

Importantly, the values of g satisfy the steady state (unperturbed) solution of the momentum (equation (4)), and the perturbed quantities ρ_1, w, and T_1 are zero before the start of simulation. Thus, there are no perturbations until they are introduced at the lower boundary. The boundary conditions on the ground surface, $z=0$, were determined by seismic measurements; the velocity perturbations w at $z=0$ were equal to the measured vertical velocities v_z of the ground surface, $w=v_z$ [Watada et al., 2006; Chum et al., 2016]. The perturbations ρ_1 and T_1 at $z=0$ were calculated from w under the simplified assumption of linearity and homogeneity. The linear assumption to calculate the ρ_1 and T_1 perturbations from the measured values of w at the lower boundary of the simulation box at $z=0$ are justified by the small values of perturbations at this boundary. Once the lower boundary conditions were defined, the evolution of w, ρ_1, and T_1 was calculated considering all the nonlinear terms in the set of inhomogeneous equations 3–5 up to the height of 400 km. The set of equations (3) to (5) was solved by the implicit finite difference method with the time and spatial resolution of 0.01 s and 40 m, respectively.

Figure 3 presents the simulated air particle velocities w at the selected altitudes. A sequence of the individual plots (Figures 3a–3i) corresponds to the altitudes of 100, 140, 160, 170, 180, 190, 200, 220, and 250 km, respectively, and shows how the N-shaped pulse forms as the wave packet propagates to higher altitudes. Time=0 corresponds to the beginning of the earthquake in all the plots. The N-shaped pulse starts forming approximately above the altitude of 100 km. The maximum absolute values of w, $|w|\sim 170$ m/s, are obtained at the altitudes around 170 km. The N-shaped pulse becomes smooth as the altitude increases. The N-shaped pulse obtained between the heights of 190 and 200 km is very similar with the pulse of w presented in Figure 1d
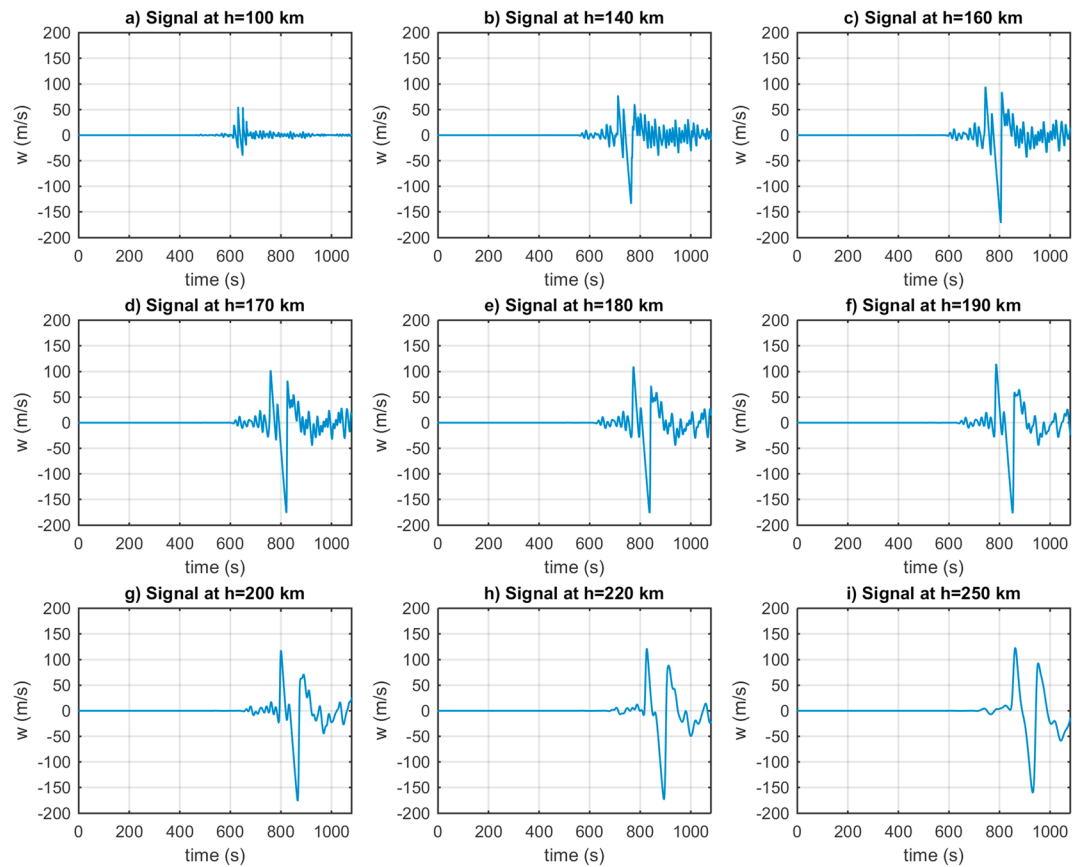
Figure 3. Results of numerical simulation (nonlinear case) for the initial perturbation $w=v_z$ on the ground at heights (a) 100, (b) 140, (c) 160, (d) 170, (e) 180, (f) 190, (g) 200, (h) 220, and (i) 250 km.

that was calculated from the measured Doppler shift. The simulated pulse for heights 190 to 200 km and the pulse derived from measurements have the similar shape, amplitude, and time of observation, i.e., about 530 s after the perturbation on the ground, displayed in Figure 1a. The heights 190 to 200 km also correspond to the height of reflection that was estimated from the measurement by ionospheric sounder (~195 km). The values of w calculated from the observed Doppler shift by equation (2) are approximately 20% smaller than those obtained in the simulation, whereas the values obtained from the measured Doppler shift by equation (1) are about 20% larger than the simulated ones. It is reasonable to assume that the measured (real) values should be a bit smaller than those obtained from the one-dimensional numerical simulation as the infrasound wave might not propagate exactly as an ideal plane wave. There might be a certain divergence of the wave front, which, together with eddy diffusion [*Hickey et al.*, 2001], might cause a partial decrease of wave energy density in the upper thermosphere/ionosphere with respect to the simulation.

In order to see the importance of nonlinear effects to form the N-shaped pulse, it is instructive to perform an identical simulation, however, with much lower initial perturbation on the ground. Results of such a simulation for the initial perturbations $w=v_z/1000$ at $z=0$ are presented in the sequence of plots in Figure 4. It is obvious that no N-shaped pulse is formed in this case. The maximum absolute velocity of air particles w is much lower than the speed of sound at all altitudes in this case, $|w| \ll c_S$. This is different from the original case, $w=v_z$, presented in Figure 3, in which w reaches several tens of percent of c_S. The speed of sound was shown in Figure 2e and was calculated by equation (6) using the atmospheric parameters obtained by the NRLMSISE-00 model.

$$c_s = \sqrt{\gamma R T_0}. \tag{6}$$

The dissipation of wave energy is mainly caused by the viscous forces and thermal conductivity that causes a heat exchange with the surrounding air [*Bass et al.*, 1984]. Therefore, the terms responsible for the dissipation
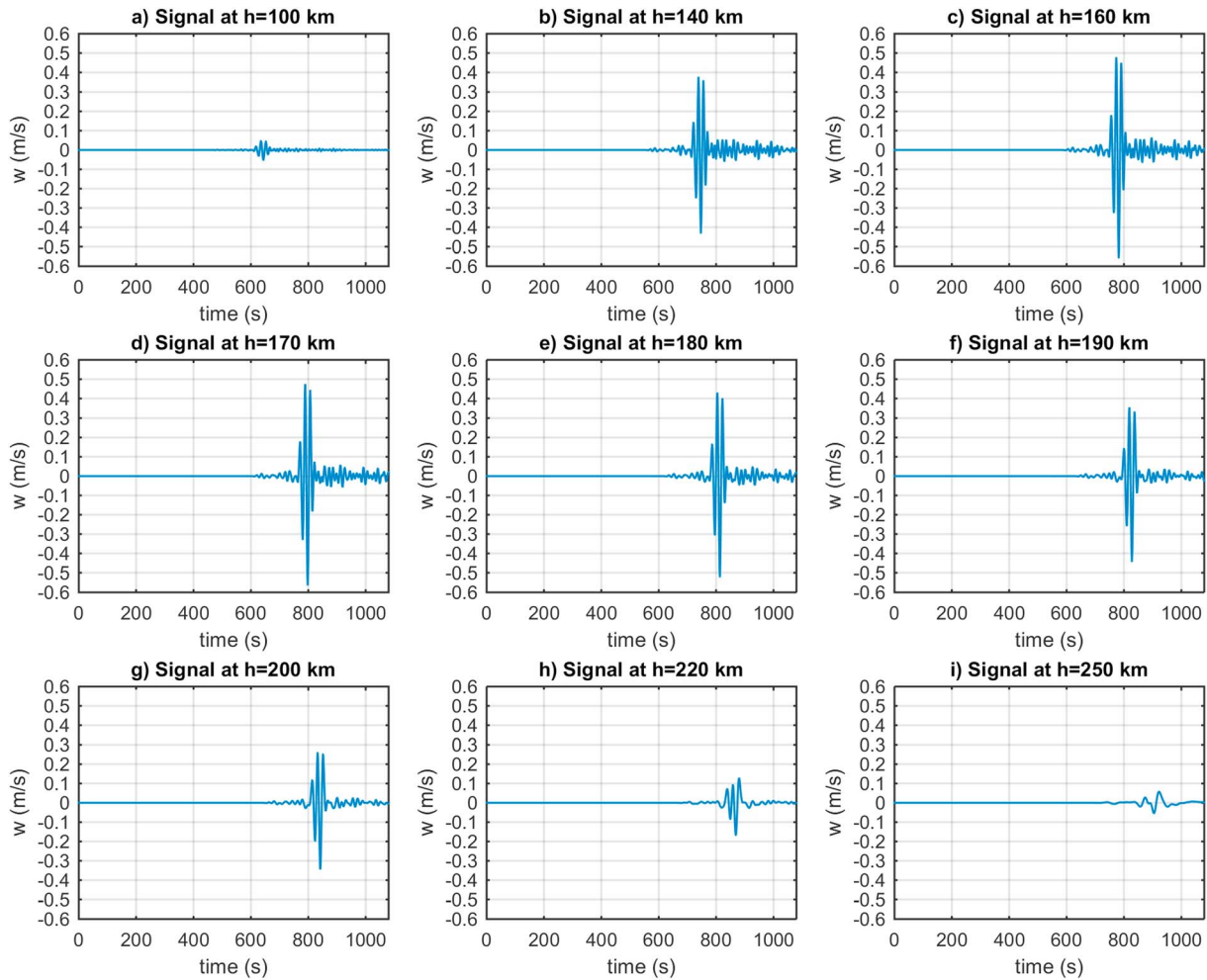
Figure 4. Results of numerical simulation (linear case) for the initial perturbation $w=v_z/1000$ on the ground at heights (a) 100, (b) 140, (c) 160, (d) 170, (e) 180, (f) 190, (g) 200, (h) 220, and (i) 250 km.

are the last terms on the right-hand sides of equations (4) and (5). As the air density ρ decreases with height, the kinematic viscosity $v=\mu/\rho$ and the dissipation increase. The second derivatives of perturbed quantities are proportional to k^2, where k is the wave vector. So, the dissipation rate and height of dissipation depends on the wave frequency [*Bass et al.*, 1984; *Blanc*, 1985]. The higher the frequency, the lower is the height of dissipation. For example, the waves at frequency of 0.05 Hz become substantially attenuated above about 150 km, in the linear case [*Chum et al.*, 2016].

It is useful to compare the dissipation of wave energy with a lossless propagation of the vertically propagating plane wave. If the plane wave propagates vertically in the inviscid atmosphere ($\mu=0$), then the energy density flux $\rho c_S w^2$ is conserved. So, as the air density decreases with height, the air particle velocity increases. Figures 5a and 5b display the attenuations A of the vertically propagating infrasound wave packets in viscous atmosphere obtained by numerical simulation at different heights calculated by equation (7) for the initial perturbations $w=v_z$ and $w=v_z/1000$ at $z=0$, respectively.

$$A = \frac{E_i}{E_G} F, \quad F = \frac{\rho_i c_{Si}}{\rho_G c_{SG}}, \tag{7}$$

where E_i is the energy of w signal (sum of the instantaneous w^2 values) in the ith height bin, and E_G is the energy of w signal in the lowest height bin. The factor F compensates the dependence of w^2 on the air density and sound speed. In the case of lossless propagation, $A=1$, at all the heights. For large initial perturbations ($w=v_z$, Figure 5a), the attenuation A decreases slowly up to the specific altitude, about 100 km in this case,
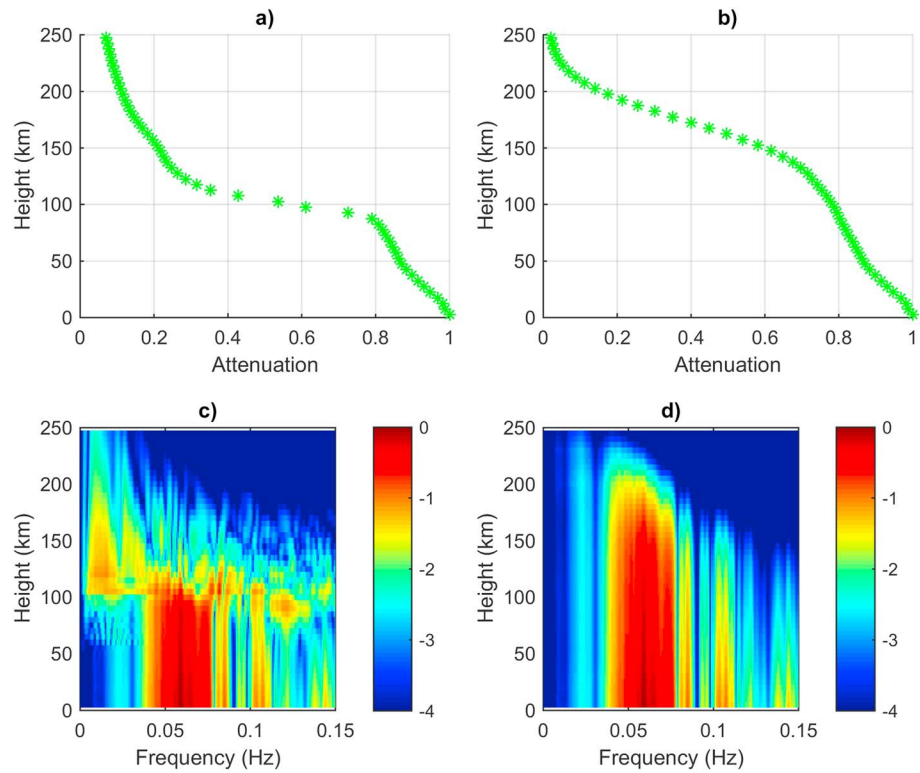
Figure 5. Attenuation and power spectral densities of air particle velocities as functions of height. (a and b) Attenuation obtained from numerical simulation for initial perturbation $w=v_z$ (nonlinear case) and $w=v_z/1000$ (linear case). (c and d) Common logarithm of normalized power spectral densities obtained from numerical simulation for initial perturbation $w=v_z$ (nonlinear case) and $w=v_z/1000$ (linear case), respectively.

at which the nonlinear effects start to play an important role. The nonlinear phenomena lead to a strong damping, decrease of A, to ensure that the density perturbations are smaller than the ambient density and that $|w| < c_s$. Besides the dissipation, a part of the energy is transformed to the lower frequencies; the frequency content is changed abruptly as can be seen in Figure 5c. The N-shaped pulse is being formed. This pulse is then relatively weakly attenuated because of its low-frequency content and can propagate to high altitudes. This is different from the linear regime of propagation ($w=v_z/1000$, Figure 5b), in which the frequency content changes smoothly with height; the higher frequencies being gradually dissipated at lower altitudes as is displayed in Figure 5d. Figures 5c and 5d show the evolution of normalized power spectral densities (PSDs) with height for the initial perturbations $w=v_z$ and $w=v_z/1000$ at $z=0$, respectively. The normalization was done as follows: First, the PSDs computed in the individual height bins were dived by their maxima to ensure that the maximum of PSD equals one in each height bin. Then, these PSDs were multiplied by A. The colors represent the common logarithm of the normalized PSDs. So, Figures 5c and 5d display both the evolution of dominant frequency and the attenuation with height. It is obvious that the N-shaped pulse that is formed above ~100 km is composed of very low frequencies and can propagate to higher altitudes compared to the wave packet propagating in the linear regime, though, initially, the nonlinear effects lead to the strong damping. It is also necessary to stress that the absolute energy is much higher for the nonlinear case than for the linear case (the normalization was done separately for both cases).

It is useful to stress that the formation of the N-shaped pulse does not depend on the specific shape and phase of the initial perturbation, provided that the initial perturbation (wave packet) is short enough (obviously, an initial perturbation in the form of sinusoidal signal with a large number of periods will not form the N-shaped pulse). Figure 6 documents that a nearly identical N-shaped pulse is formed for the inverted initial perturbation, $w=-v_z$.
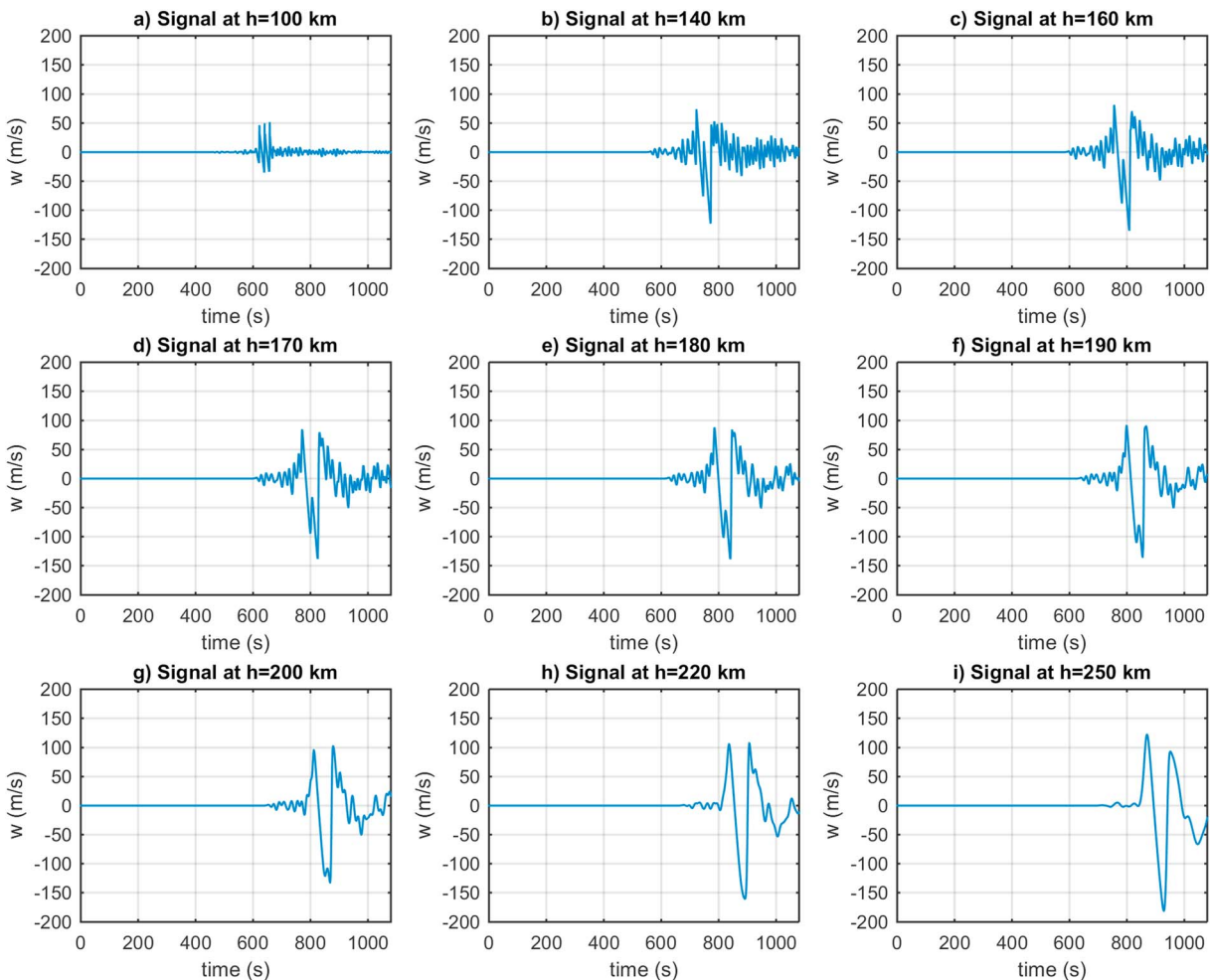
Figure 6. Results of numerical simulation (nonlinear case) for the inverted initial perturbation, $w=-v_z$, on the ground at heights (a) 100, (b) 140, (c) 160, (d) 170, (e) 180, (f) 190, (g) 200, (h) 220, and (i) 250 km.

5. Discussion

It was shown that the N-shaped pulse is formed in the upper atmosphere if the initial perturbation, caused by the vertical movement of the ground surface, has large amplitude so that the nonlinear processes start to play an important role and significantly change the shape of propagating wave packet and its frequency content (Figures 3, 5c, and 6). It was demonstrated that for the small initial amplitudes, without the nonlinear effects, the N-shaped pulse is not formed, and the shape and frequency content of the wave packet change smoothly with height (Figures 4 and 5d); the frequency content changes smoothly as the higher frequencies are attenuated earlier, at lower heights. The numerical simulation is in good agreement with the measurement at the height of about 195 km that was performed by CDSS located approximately 800 km from the epicenter of the Illapel earthquake.

It is useful to note that the formation of the N-shaped pulse was not reported at regions far from the epicenter (several thousand of kilometers) as the initial perturbations were not large enough to produce significant nonlinear effects. *Chum et al.* [2012] found high cross-correlation coefficients (above 0.9) between v_z and w (f_D) at the height of about 210 km measured by CDSS in the Czech Republic for the 2011 Tohoku earthquake. Similar shapes of wave packets and frequency contents of v_z and w (f_D) fluctuations were also observed for the 2015 Nepal earthquake by the CDSS in the Czech Republic and Taiwan [*Chum et al.*, 2016]. At the same time, these studies showed that the infrasound was generated from the seismic waves locally and propagated quasi-vertically upward. The coseismic perturbations caused by vertically propagating infrasound waves were also confirmed by independent sounding techniques; *Maruyama and Shinagawa* [2014] showed

that the disturbances observed in the ionograms are consistent with the ionospheric perturbations generated by the vertically propagating infrasound. *Liu et al.* [2016] used collocated measurements by seismometers, infrasound sensors, magnetometers, continuous Doppler sounding, and dual-frequency GPS receivers in Taiwan to demonstrate that the time delays between observations of coseismic disturbances at various heights are consistent with the vertically propagating infrasound waves generated locally in Taiwan by the vertical component of seismic waves triggered by the 2011 Tohoku earthquake.

We do not know about any other report of the coseismic disturbances in the form of the N-shaped pulse based on observations by CDSS in the vicinity of a strong earthquake (approximately up to horizontal distance of 1000 km from the epicenter of $M_w > 7$ earthquake). To the best of our knowledge, the reports of the coseismic N-shaped pulses in the vicinity of strong earthquakes were only based on the observations of TEC variations from dual GPS receivers [*Afraimovich et al.*, 2001; *Astafyeva and Heki*, 2009; *Astafyeva et al.*, 2011; *Reddy and Seemala*, 2015]. As was discussed in section 1, TEC is an integrated value of electron densities, so it is difficult to compare its fluctuations with the waveform at a specific altitude. *Afraimovich et al.* [2001] tried to explain the formation of the N-shaped pulse in the upper atmosphere and ionosphere. They linearly summed obliquely propagating infrasound waves that originated at different places on the ground to get the N-shaped pulse using an approximation of linear geometrical acoustics. They did not use real seismic measurements to define the initial conditions; they used a simple model of the initial perturbations that was based on rectangular velocity impulse. Contrary, our work is based on the nonlinear numerical solution of differential equations for compressible gas, including the viscosity and thermal conductivity; the initial conditions were defined by the real measurements of v_z. Our approach is similar to the simulations performed by *Maruyama and Shinagawa* [2014]. They, however, used the initial perturbations of v_z of several mm/s on the ground (in our case, the initial perturbation reached almost 40 mm/s). They did not show the formation of the N-shaped pulse and did not discuss the nonlinear effects. The nonlinear effects on infrasound propagation and attenuation were discussed by *Krasnov et al.* [2007]. However, they used an analytical approach, rather than the numerical solution of differential equations. In addition, they used long artificial sinusoidal signals as the initial perturbation on the ground, and their work was not directly linked to an earthquake.

A number of independent reports mentioned in the discussion above demonstrated that the propagation of infrasound generated by seismic waves is to a good approximation vertical. More precisely, because of supersonic speed of seismic waves, it is expected that the infrasound waves start to propagate with a small deviation from vertical, with the zenith angle $a = \mathrm{asin}(c_{s0}/c_G)$, where c_{s0} is the speed of sound above the ground, and c_G is the horizontal speed of seismic waves [*Chum et al.*, 2016, and references therein]. As $c_{s0} \ll c_G$, a is usually less than about 7°. A more complicated situation might be around the epicenter, where the seismic waves start forming and propagate in different directions; consequently, the infrasound waves can be generated with various directions of the wave vectors. It is therefore useful to investigate whether the rays from the epicenter can reach the observation point at 800 km horizontal distance and height of about 195 km. Figure 7 shows the results of ray tracing simulation performed in polar coordinates for the infrasound waves started on the ground at epicenter (horizontal distance=0) with different initial zenith angles a (a=0 by red, a=10° by yellow, a=20° by green, a=30° by blue, and a=40° by magenta). The sound speed was obtained from the NRLMSISE-00 model; the speed of neutral winds was estimated from HWM14 model [*Drob et al.*, 2015]. Obviously, the rays from the epicenter do not reach the observation point at 800 km horizontal distance and height of about 195 km (Figure 7a). In addition, the oblique rays are attenuated more than the quasi-vertical rays (Figure 7d), especially at altitudes above approximately 150 km, as their paths in highly dissipative medium are longer. The attenuation along the ray trajectories was calculated for frequency of 0.06 Hz under the linear approximation using the analytic model described by *Chum et al.* [2012]. The rays started with a larger than about 26°, in this case, undergo a reflection from the lower troposphere, and could be probably observed on the ground [*Le Pichon et al.*, 2002]. The results of ray tracing, together with the discussion related to vertical propagation above, thus justify the approximation of vertical propagation used in the numerical simulation to explain the formation of the N-shaped pulse; the results of numerical simulations are in good agreement with observation.

The present study contributes to a better understanding of the coupling mechanisms between the lower atmosphere and upper atmosphere and ionosphere, including coupling from processes in the solid Earth. It helps understanding the atmospheric and ionospheric variability on short time scales (tens of seconds up to several minutes) in general. The proper understanding of atmospheric and ionospheric perturbations
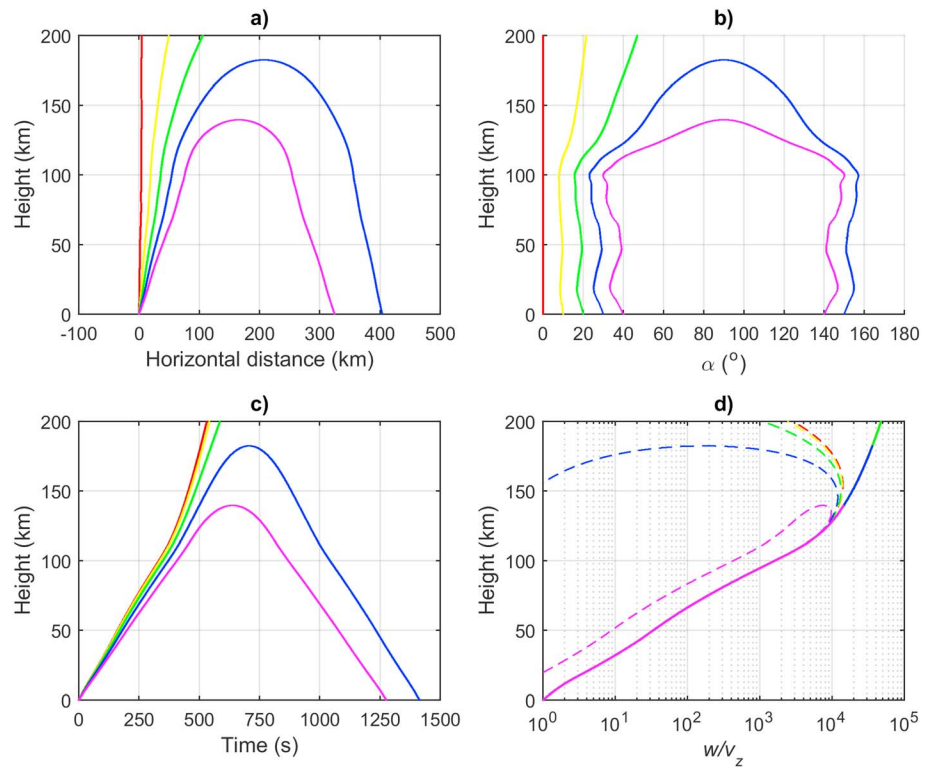
Figure 7. Ray tracing results for the infrasound waves generated with the initial zenith angles $\alpha=0$ (red), $\alpha=10°$ (yellow), $\alpha=20°$ (green), $\alpha=30°$ (blue), and $\alpha=40°$ (magenta). (a) Horizontal distances from the epicenter versus height. (b) Evolution of α with height. (c) Height as a function of time. (d) w/v_z ratios as functions of height for lossless propagation (solid) and for the attenuation calculated for frequency of 0.06 Hz by analytic model (dashed).

might potentially find practical applications, e.g., in tsunami warning systems. As the atmospheric waves propagate faster than the tsunami in ocean (around 200 m/s at deep water), there is a theoretical possibility to use a detection of atmospheric and ionospheric perturbations in tsunami warning systems, provided that the epicenter is far enough from the coast [*Arai et al.*, 2011; *Kakinami et al.*, 2012]. Obviously, the atmospheric and ionospheric observations would form only a part of the warning system. A correct understanding of the processes in the Earth-ocean-atmosphere system, including the changes of the shapes and spectral content of the waveforms owing to nonlinear effects and attenuation, and correct distinguishing of cotsunami perturbations from perturbations caused by other sources will be necessary to apply these methods.

6. Conclusions

The coseismic perturbations in the ionosphere, generated by the 16 September 2015, Illapel earthquake, were investigated both experimentally and theoretically, using numerical solution of the compressional fluid equations in the viscous atmosphere. It was shown that the N-shaped perturbations observed in the ionosphere close to the epicenter of strong earthquake (up to about horizontal distance of 1000 km) can be explained by nonlinear effects on quasi-vertically propagating infrasound waves. When formed, the N-shaped pulse was composed of low-frequency infrasound waves with dominant period of 2 min; the original wave packet was mainly composed of the frequencies around 0.06 Hz (period ~17 s). The N-shaped pulse can propagate, with observable amplitudes, up to the altitudes of the F_2 peak (around 250 to 300 km) before being dissipated. The results of numerical solution of the nonlinear compressional fluid equations in 1-D, along the vertical axis, are in a good agreement with the air particle velocities observed by continuous Doppler sounding at about 800 km distance from the epicenter and height of about 195 km.

References

Afraimovich, E. L., N. P. Perevalova, A. V. Plotnikov, and A. M. Uralov (2001), The shock-acoustic waves generated by the earthquakes, *Ann. Geophys.*, *19*(4), 395–409, doi:10.5194/angeo-19-395-2001.

Arai, N., M. Iwakuni, S. Watada, Y. Imanishi, T. Murayama, and M. Nogami (2011), Atmospheric boundary waves excited by the tsunami generation related to the 2011 great Tohoku-Oki earthquake, *Geophys. Res. Lett.*, *38*, L00G18, doi:10.1029/2011GL049146.

Artru, J., T. Farges, and P. Lognonné (2004), Acoustic waves generated from seismic surface waves: Propagation properties determined from Doppler sounding observations and normal-mode modeling, *Geophys. J. Int.*, *158*, 1067–1077, doi:10.1111/j.1365-246X.2004.02377.x.

Astafyeva, E., and K. Heki (2009), Dependence of wave form of near-field coseismic ionospheric disturbances on focal mechanisms, *Earth Planet Space*, *61*, 939–943, doi:10.1186/BF03353206.

Astafyeva, E., P. Lognonne, and L. Rolland (2011), First ionospheric images of the seismic fault slip on the example of the Tohoku-Oki earthquake, *Geophys. Res. Lett.*, *38*, L22104, doi:10.1029/2011GL049623.

Barrientos, S. (2015), Informe Técnico Terremoto Illapel 16 Septiembre 2015 [in Spanish]. [Available at http://www.csn.uchile.cl/wp-content/uploads/2015/12/Informe_Tecnico_terremoto_Illapel_SB.pdf.]

Bass, H. E., L. C. Sutherland, J. Piercy, and L. Evans (1984), Absorption of sound by the atmosphere, *in Physical Acoustics*, vol. 17, edited by W. P. Mason and R. N. Thurston, chap. 3, pp. 145–232, Academic, New York.

Blanc, E. (1985), Observations in the upper atmosphere of infrasonic waves from natural or artificial sources: A summary, *Ann. Geophys.*, *3*, 673–688.

Bolt, B. A. (1964), Seismic air waves from the great 1964 Alaskan earthquake, *Nature*, *202*, 1095–1096, doi:10.1038/2021095a0.

Calais, E., and J. B. Minster (1995), GPS detection of ionospheric perturbations following the January 17 1994, Northridge earthquake, *Geophys. Res. Lett.*, *22*, 1045–1048, doi:10.1029/95GL00168.

Chum, J., F. Hruska, J. Zednik, and J. Lastovicka (2012), Ionospheric disturbances (infrasound waves) over the Czech Republic excited by the 2011 Tohoku earthquake (2012), *J. Geophys. Res.*, *117*, A08319, doi:10.1029/2012JA017767.

Chum, J., et al. (2014), Propagation of gravity waves and spread F in the low-latitude ionosphere over Tucumán, Argentina, by continuous Doppler sounding: First results, *J. Geophys. Res. Space Physics*, *119*, 6954–6965, doi:10.1002/2014JA020184.

Chum, J., Y.-J. Liu, J. Laštovička, J. Fišer, Z. Mošna, J. Baše, and Y. Y. Sun (2016), Ionospheric signatures of the April 25, 2015 Nepal earthquake and the relative role of compression and advection for Doppler sounding of infrasound in the ionosphere, *Earth Planets Space*, *68*, 24, doi:10.1186/s40623-016-0401-9.

Dalgarno, A., and F. J. Smith (1962), The thermal conductivity and viscosity of atomic oxygen, *Planet. Space Sci.*, *9*, 1–2, doi:10.1016/0032-0633(62)90064-8.

Davies, K., and D. M. Baker (1965), Ionospheric effects observed around the time of the Alaskan earthquake of March 28, 1964, *J. Geophys. Res.*, *70*(9), 2251–2253, doi:10.1029/JZ070i009p02251.

Donn, W. L., and E. S. Posmentier (1964), Ground-coupled air waves from the great Alaskan earthquake, *J. Geophys. Res.*, *69*, 5357–5361, doi:10.1029/JZ069i024p05357.

Drob, D. P., et al. (2015), An update to the Horizontal Wind Model (HWM): The quiet time thermosphere, *Earth Space Sci.*, *2*, 301–319, doi:10.1002/2014EA000089.

Heki, K., and J. Ping (2005), Directivity and apparent velocity of the coseismic ionospheric disturbances observed with a dense GPS array, *Earth Planet. Sci. Lett.*, *236*, 845–855, doi:10.1016/j.epsl.2005.06.010.

Hickey, M. P., G. Schubert, and R. L. Walterscheid (2001), Acoustic wave heating of the thermosphere, *J. Geophys. Res.*, *106*(A10), 21,543–21,548, doi:10.1029/2001JA000036.

Kakinami, Y., M. Kamogawa, Y. Tanioka, S. Watanabe, A. R. Gusman, J.-Y. Liu, Y. Watanabe, and T. Mogi (2012), Tsunamigenic ionospheric hole, *Geophys. Res. Lett.*, *39*, L00G27, doi:10.1029/2011GL050159.

Kherani, E. A., L. Rolland, P. Lognonné, A. Sladen, V. Klausner, and E. R. de Paula (2016), Traveling ionospheric disturbances propagating ahead of the Tohoku-Oki tsunami: A case study, *Geophys. J. Int.*, *204*, 1148–1158, doi:10.1093/gji/ggv500.

Krasnov, V. M., Y. Drobzheva, and J. Lastovicka (2007), Acoustic energy transfer to the upper atmosphere from sinusoidal sources and a role of non-linear processes, *J. Atmos. Sol. Terr. Phys.*, *69*, 1357–1365, doi:10.1016/j.jastp.2007.04.011.

Lastovicka, J., J. Base, F. Hruska, J. Chum, T. Sindelarova, J. Horalek, J. Zednik, and V. Krasnov (2010), Simultaneous infrasonic, seismic, magnetic and ionospheric observations in an earthquake epicentre, *J. Atmos. Sol. Terr. Phys.*, *72*, 1231–1240, doi:10.1016/jastp.2010.08.005.

Le Pichon, A., J. Guilbert, A. Vega, M. Garce˙s, and N. Brachet (2002), Ground-coupled air waves and diffracted infrasound from the Arequipa earthquake of June 23, 2001, *Geophys. Res. Lett.*, *29*(18), 1886, doi:10.1029/2002GL015052.

Liu, J. Y., Y. B. Tsai, S. W. Chen, C. P. Lee, Y. C. Chen, H. Y. Yen, W. Y. Chang, and C. Liu (2006), Giant ionospheric disturbances excited by the M9.3 Sumatra earthquake of 26 December 2004, *Geophys. Res. Lett.*, *33*, L02103, doi:10.1029/2005GL023963.

Liu, J. Y., et al. (2016), The vertical propagation of disturbances triggered by seismic waves of the 11 March 2011 *M*9.0 Tohoku earthquake over Taiwan, *Geophys. Res. Lett.*, *43*, 1759–1765, doi:10.1002/2015GL067487.

Liu, J.-Y., C.-H. Chen, C.-H. Lin, H.-F. Tsai, C.-H. Chen, and M. Kamogawa (2011), Ionospheric disturbances triggered by the 11 March 2011 M9.0 Tohoku earthquake, *J. Geophys. Res.*, *116*, A06319, doi:10.1029/2011JA016761.

Maruyama, T., and H. Shinagawa (2014), Infrasonic sounds excited by seismic waves of the 2011 Tohoku-Oki earthquake as visualized in ionograms, *J. Geophys. Res. Space Physics*, *119*, 4094–4108, doi:10.1002/2013JA019707.

Reddy, C. D., and G. K. Seemala (2015), Two-mode ionospheric response and Rayleigh wave group velocity distribution reckoned from GPS measurement following M_w 7.8 Nepal earthquake on 25 April 2015, *J. Geophys. Res. Space Physics*, *120*, 7049–7059, doi:10.1002/2015JA021502.

Reinisch, B. W., X. Huang, I. A. Galkin, V. Paznukhov, and A. Kozlov (2005), Recent advances in real-time analysis of ionograms and ionospheric drift measurements with digisondes, *J. Atmos. Sol. Terr. Phys.*, *67*, 1054–1062, doi:10.1016/j.jastp.2005.01.009.

Rishbeth, H. (1997), The ionospheric *E*-layer and *F* layer dynamos—A tutorial review, *J. Atmos. Sol. Terr. Phys.*, *59*, 1873–1880.

Rolland, L. M., G. Occhipinti, P. Lognonné, and A. Loevenbruck (2010), Ionospheric gravity waves detected offshore Hawaii after tsunamis, *Geophys. Res. Lett.*, *37*, L17101, doi:10.1029/2010GL044479.

Sutherland, L. C., and H. E. Bass (2004), Atmospheric absorption in the atmosphere up to 160 km, *J. Acoust. Soc. Am.*, *115*, 1012–1032, doi:10.1121/1.1631937.

Tilmann, F., et al. (2016), The 2015 Illapel earthquake, central Chile: A type case for a characteristic earthquake?, *Geophys. Res. Lett.*, *43*, 574–583, doi:10.1002/2015GL066963.

Vadas, S. L., and D. C. Fritts (2005), Thermospheric responses to gravity waves: Influences of increasing viscosity and thermal diffusivity, *J. Geophys. Res.*, *110*, D15103, doi:10.1029/2004JD005574.

Watada, S., T. Kunugi, K. Hirata, H. Sugioka, K. Nishida, S. Sekiguchi, J. Oikawa, Y. Tsuji, and H. Kanamori (2006), Atmospheric pressure chase associated with the 2003 Tokachi-Oki earthquake, *Geophys. Res. Lett.*, *33*, L24306, doi:10.1029/2006GL027967.